Giant bandwidth tailoring of perfect light absorbers: Empowered by quasibound states in the continuum

Jie Wang [1,2,*] Xiao Wang,[3,4] Zhongjie Zhu,[1] Hongwei Zhao,[1,3] and Min Chen[1,3,†]

[1]*Shanghai Synchrotron Radiation Facility, Shanghai Advanced Research Institute, Chinese Academy of Sciences, Shanghai 201210, China*

[2]*State Key Laboratory of Surface Physics and Department of Physics, Fudan University, Shanghai 200433, China*

[3]*Shanghai Institute of Applied Physics, Chinese Academy of Sciences, Shanghai 201800, China*

[4]*University of Chinese Academy of Sciences, Beijing 100049, China*

(Received 26 July 2023; revised 15 November 2023; accepted 15 November 2023; published 30 November 2023)

The ability to adjust the absorption bandwidth of an optical absorber with high efficiency can facilitate the development of novel photonic and optoelectronic devices. In this work, based on the temporal coupled-mode theory, we establish a connection between the absorption bandwidth of an absorber and radiation engineering with the symmetry-broken quasi-BIC and propose a BIC-inspired strategy to tailor light absorption at critical coupling with a wide range of functionality. Based on this, the manipulation of the broadband or narrow-band quasi-BIC-governed graphene perfect absorber is realized, and the corresponding absorption bandwidth at critical coupling can be drastically adjusted by more than three orders of magnitude. Moreover, we predict and verify the quadratic scalability of the absorption bandwidth on the asymmetry parameter of the quasi-BIC structure, essentially arising from the powerful physics of BIC in radiation engineering. Present work not only provides a profound physical insight into the tailoring functionalities of radiation and in particular absorption by BIC, but also affords new possibilities for research into active optical devices.

DOI: 10.1103/PhysRevB.108.205428

I. INTRODUCTION

Light absorption is of fundamental significance in many technological applications including photonic [1,2] and optoelectronic devices [3,4]. To decrease material consumption and improve the integrability, it is highly desirable to design the high-performance absorber with nanoscale thickness and low volume, which meanwhile could also inevitably weaken the ability to confine light. Recent studies have demonstrated through coupling with carefully designed resonant structures, such as photonic crystal (PhC) slab [5–8], metamaterial and metasurface [9–12], or plasmonic structure [13–16], the efficiency of the absorbing material could be enhanced. The physical interpretations of these works can be attributed to critical coupling concept that the optimal absorption could be realized when absorption rate γ_a of the absorbing material matches radiation rate γ_r of the photonic resonator. However, many works have concentrated on the absorption enhancement while little attention has been paid to the bandwidth of the absorption. Usually, the way of multimode resonators is used to realize broadband absorption [17–19], and a high-Q optical resonance is used to realize narrow-band absorption [20–22]. These works fall short of providing satisfactory enhancement of absorption and bandwidth tunability, meanwhile mainly rely on surveying geometrical features of structure to tailor the bandwidth of an absorber. Obviously, to find a simple and general way to manipulate light absorption performance is certainly desired.

With the concept of critical coupling, the light absorption performance is essentially linked with the radiation engineering of the resonant structure. To tailor the light absorption, the resonant structure with wide radiation capability is needed. Benefiting from low intrinsic loss, all-dielectric structures have been shown to be a promising platform for advanced control and manipulation of light governed by radiation leakage only [23–25]. Especially, the recently emerged concept of bound states in the continuum (BICs) in all-dielectric nanophotonics enables a new solution for effective engineering of radiation behavior [26–29]. BICs are peculiar states with the energy lying in the delocalized states in the continuum, but counter-intuitively cannot couple with the radiating channels and remain perfectly localized states in space with an infinite lifetime. Through altering structure parameters or introducing defects and perturbations to break the structural symmetries, BICs could collapse to quasi-BICs with finite lifetime and radiation capability [23]. This functionality is highly desirable and would hold great potential in tailoring light absorption performance.

In this paper, a BIC-inspired strategy for designing an optimal absorber with widely tailored functionality of absorption bandwidth is presented. We employ the temporal coupled-mode theory (CMT) to establish a close link between the absorption bandwidth of an absorber at critical coupling condition and a symmetry-broken quasi-BIC. It shows that to achieve perfect absorption, a symmetric-broken quasi-BIC resonance structure with a single radiation port is preferably required. To tailor absorption bandwidth, it needs to adjust γ_r

*wangj@sari.ac.cn; jwang14@fudan.edu.cn

†chenm@sari.ac.cn

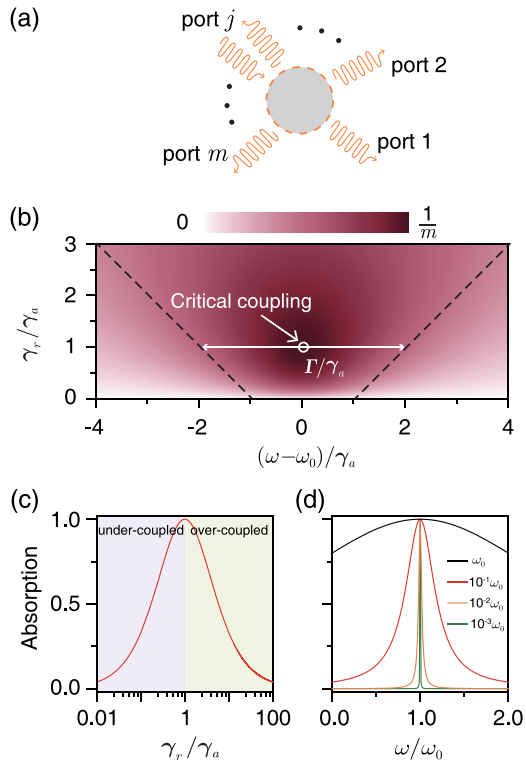

FIG. 1. (a) Schematic of a single-mode optical resonator excited from port j and coupled out through m free-space ports. The orange arrows indicate the incoming and outgoing waves of each port. (b) Absorption performance of a resonator with m ports. Maximum absorption occurs at the resonance frequency and critical coupling condition $\gamma_r = \gamma_a$, which is marked by hollow dot. The white arrow corresponds to the absorption bandwidth at critical coupling. (c) Absorption at the resonance frequency of a single port resonator as a function of γ_r/γ_a. (d) Absorption at critical coupling of a single port resonator as a function of frequency.

and γ_a at critical coupling simultaneously over a wide range. It is found that γ_r of symmetry-broken quasi-BIC with a single radiation port can be adjusted significantly by the structure asymmetry parameter. γ_a can be controlled by changing the amount of the absorbing material and its position in the resonance structure. Based on that, the absorption bandwidth of an absorber can be tailored by more than three orders of magnitude while maintaining perfect absorption. Interestingly, the quadratic scalability of the absorption bandwidth on the asymmetry parameter, governed by the powerful physics of BIC in radiation engineering, is predicted and verified. This work reveals the mighty capability of BIC for radiation and absorption engineering and would provide conceptual strategy to develop perspective optical devices such as light harvesting and emitting devices, sensors, detectors, and modulators.

II. THEORETICAL ANALYSIS

To reveal the physical property of the optimal absorption of an absorber, we first turn to a generalized resonator model of the CMT, shown in Fig. 1(a). The diagram considers a single-mode optical resonator, coupled to input $\mathbf{S}_+$ and output $\mathbf{S}_-$ waves with m ports. The dynamic equations for the amplitude a of the resonance mode can be described by the following form [30–32]:

$$\frac{da}{dt} = -i\omega_0 a - (\gamma_r + \gamma_a)a + (\langle d|^*)|s_+\rangle, \tag{1}$$

$$|s_-\rangle = C|s_+\rangle + |d\rangle a, \tag{2}$$

where ω_0 is the resonant frequency, γ_r represents the external radiation rate and γ_a is the intrinsic dissipative rate mainly originating from material absorption, respectively. It should be noted that the CMT theory is strictly valid only when the resonance width is far smaller than the resonance frequency. The vectors $|s_\pm\rangle = (s_{1\pm}, s_{2\pm}, \ldots, s_{m\pm})^T$ and $|d\rangle = (d_1, d_2, \ldots, d_m)^T$ contain the amplitude of the flux of input (+)/output (−) plane waves and the coupling coefficient from the resonance to each port. Note that the mode and wave amplitudes are normalized such that $|a|^2$ and $\langle s_\pm|s_\pm\rangle$ represent the energy stored in the resonance and power carried by the input/output wave, respectively. C is a unitary matrix describing the direct response between input and output waves in the nonresonant case, $CC^+ = I$. Under excitation from the arbitrary port, for example, with input from s_{j+}, the amplitude of the resonance mode can be derived as

$$a = \frac{d_j s_{j+}}{-i(\omega - \omega_0) + (\gamma_r + \gamma_a)}. \tag{3}$$

As an essential consequence of time-reversal symmetry and energy conservation, the radiation rate γ_r cannot be arbitrary (or even geometrical) factor and is constrained by the coupling coefficients $|d\rangle$. It obeys the constrains with $\langle d|d\rangle = 2\gamma_r$ and $C|d\rangle^* = -|d\rangle$. Then the light absorption of the optical resonator with input from port j can be derived as

$$A = \frac{\langle s_+|s_+\rangle - \langle s_-|s_-\rangle}{\langle s_+|s_+\rangle} = \frac{2\gamma_a a^* a}{\langle s_+|s_+\rangle}$$
$$= \frac{2\gamma_a d_j^* d_j}{(\omega - \omega_0)^2 + (\gamma_a + \gamma_r)^2}. \tag{4}$$

We further assume the resonance mode coupled to each port with the same rate, it has $d_j^* d_j = 2\gamma_r/m$. Therefore, we have a simple expression for light absorption of an optical resonator with m ports,

$$A = \frac{1}{m}\frac{4\gamma_a\gamma_r}{(\omega - \omega_0)^2 + (\gamma_a + \gamma_r)^2}. \tag{5}$$

Obviously, the absorption formula exhibits a symmetric Lorentzian lineshape, shown in Fig. 1(b). It shows that the absorption performance is mainly determined by four parameters, m, ω_0, γ_a, and γ_r. It can be seen that when further away from ω_0, i.e., $|\omega - \omega_0| \gg 0$, the absorption vanishes, which implies the effect of resonance-enhanced absorption. The absorption peak of value A_0 happens on resonance $\omega = \omega_0$, $A_0 = 4/[m(\gamma_r/\gamma_a + \gamma_a/\gamma_r + 2)]$. It can be seen that A_0 is determined by the ratio between γ_r and γ_a. When $\gamma_r = \gamma_a$, the absorption of a single-mode resonator with m ports reaches its maximum

$$A_{\max} = 1/m. \tag{6}$$

This is so-called critical coupling [33], shown with a white hollow dot in Fig. 1(b). It shows that the maximum absorption

of an optical resonator is inversely proportional to the number of its ports. The perfect absorption can be realized for a single-port absorber with critical coupling $\gamma_r = \gamma_a$, shown in Fig. 1(c). Moreover, the absorption bandwidth can be obtained. The absorption bandwidth Γ^{FWHM} is defined as the full width at half maximum (FWHM). Assuming the half-maximum absorption $A_0/2$ occurs at the frequency ω_1, it has $A_0/2 = 4\gamma_a\gamma_r/[m(\omega_1 - \omega_0)^2 + m(\gamma_a + \gamma_r)^2]$. The absorption bandwidth can be achieved as

$$\Gamma^{\mathrm{FWHM}} = 2|\omega_1 - \omega_0| = 2(\gamma_a + \gamma_r). \tag{7}$$

It indicates that Γ^{FWHM} is independent of the number of ports, but depends on the sum of two rates, shown with white double arrow line in Fig. 1(b).

To summarize, the absorption efficiency of a resonant absorber is related to the number of its ports m and the ratio of two rates γ_r/γ_a. The number of ports m naturally determines the upper limit of absorption, and whether this upper limit can be achieved is determined by γ_r/γ_a. The absorption bandwidth Γ^{FWHM} is proportional to $\gamma_r + \gamma_a$. The larger (smaller) $\gamma_r + \gamma_a$ is, the wider (narrower) Γ^{FWHM} will be and vice versa. Specifically, the absorption performance of four cases with $\gamma_r = 10^{-3}\omega_0$, $10^{-2}\omega_0$, $10^{-1}\omega_0$, and ω_0 for a single-port resonator at critical coupling is shown in Fig. 1(d). It is found that the absorption bandwidth can be dramatically tailored with perfect absorption. Thus, to manipulate absorption bandwidth while maintaining high absorption efficiency of an absorber, γ_r and γ_a need to be simultaneously adjusted at critical coupling. At critical coupling condition,

$$\Gamma^{\mathrm{FWHM}} = 4\gamma_a = 4\gamma_r. \tag{8}$$

γ_a represents the intrinsic absorption coefficient of an absorber and can be adjusted through changing the amount of the absorbing materials. γ_r links to the optical mode of a resonator and its structure parameters. γ_r should be engineered as widely as possible to match γ_a. Therefore, the radiation capability of the resonant structure directly dominates the absorption bandwidth.

The BIC-inspired mechanism makes it possible to fully engineer light radiation γ_r. Especially, the quasi-BIC Fano resonance corresponding to a collapse of the symmetry-protected BIC due to a broken structural symmetry has priority. An ideal symmetry-protected BIC exists within the continuum, but without any radiation ports to the free space due to symmetry-induced destructive interference, namely $\gamma_r = 0$. Once a perturbation δ is introduced to break the in-plane inversion symmetry, the radiation ports are opened and such a BIC transforms into a quasi-BIC with $\gamma_r > 0$. Based on perturbation theory, a universal behavior of the quadratic dependence of γ_r of quasi-BIC on the asymmetry parameter δ has been demonstrated [23,34],

$$\gamma_r = \gamma_0\delta^2, \tag{9}$$

where γ_0 is a constant independent from δ. Substituting Eq. (9) to Eq. (8), the dependence of Γ^{FWHM} on δ at critical coupling can be obtained as

$$\Gamma^{\mathrm{FWHM}} \propto \delta^2. \tag{10}$$

It shows that Γ^{FWHM} at critical coupling also exhibits the quadratic dependence on δ, similar to that of γ_r, closely

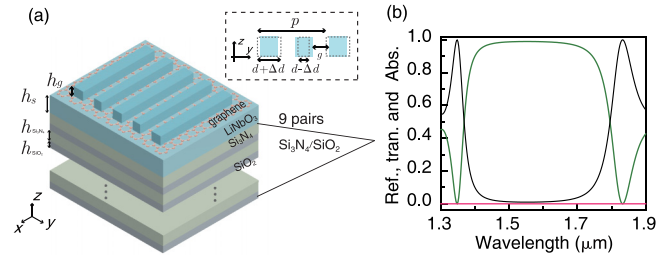

FIG. 2. (a) Schematic of the quasi-BIC structure integrated with graphene. The quasi-BIC structure is constructed by 1D symmetry-broken dimerized $LiNbO_3$ (LN) lattice structure deposited atop a multilayer dielectric Bragg reflector (DBR) with nine pairs of Si_3N_4/SiO_2. The structure has $p = 800\,\mathrm{nm}$, $d = 0.25p$, $g = 0.25p$, $h_g = 220\,\mathrm{nm}$, $h_s = 270\,\mathrm{nm}$, $h_{\mathrm{Si_3N_4}} = 192\,\mathrm{nm}$, and $h_{\mathrm{SiO_2}} = 268\,\mathrm{nm}$. The width perturbation Δd is used to break in-plane inversion symmetry. The asymmetry parameter δ is denoted by $\delta = \Delta d/d$. (b) Reflection (green curve), transmission (black curve) and absorption (red curve) spectra of the DBR under normal incidence.

associated with the physics of BIC. Thus, this universal rule provides a simple but rigorous way to accurately manipulate the absorption bandwidth of an optical absorber with perfect efficiency.

The following is an example of a model structure in which a quasi-BIC photonic crystal slab structure implemented on a multilayer dielectric Bragg reflector (DBR) is employed to tailor the absorption bandwidth of the absorbing material graphene. This structure has only a single-port radiation capability due to the suppression of transmission by the DBR, and $A_{\max} = 100\%$. Based on this quasi-BIC system, it is shown how to tailor the absorption bandwidth of an absorber with perfect absorption.

III. STRUCTURE DESIGN AND NUMERICAL MODEL OF QUASI-BIC STRUCTURE

Specifically to construct quasi-BIC structure, 1D symmetry-broken dimerized lattice structure deposited atop a DBR is adopted, as shown in Fig. 2(a). 1D symmetry-broken dimerized lattice structure consists of two layers: the upper layer is dimerized $LiNbO_3$ (LN) grating with height h_g and the lower layer is unetched LN film with thickness h_s. The unit lattice of the dimerized LN grating consists of two adjacent stripes separated by an air gap of width g. The periodicity of the unit lattice of the dimerized LN grating is p, and the widths of two stripes are $d + \Delta d$ and $d - \Delta d$, respectively. The width perturbation Δd is used to break in-plane inversion symmetry. The asymmetry parameter δ is denoted by $\delta = \Delta d/d$. The DBR consists of nine pairs of Si_3N_4/SiO_2 layers, where the thicknesses of Si_3N_4 and SiO_2 layers are $h_{\mathrm{Si_3N_4}}$ and $h_{\mathrm{SiO_2}}$, respectively. The numerical simulations are conducted by 2-D rigorous coupled-wave analysis (Diffract MODE, RSOFT) [35]. In the calculations, the plane wave source is incident along the $-z$ direction with its polarization parallel to the x direction and the periodic boundary condition is set in the y direction. The refractive indices of Si_3N_4 and SiO_2 are set as 2.02 and 1.45, respectively. The permittivity of LN are set the same as Ref. [20].

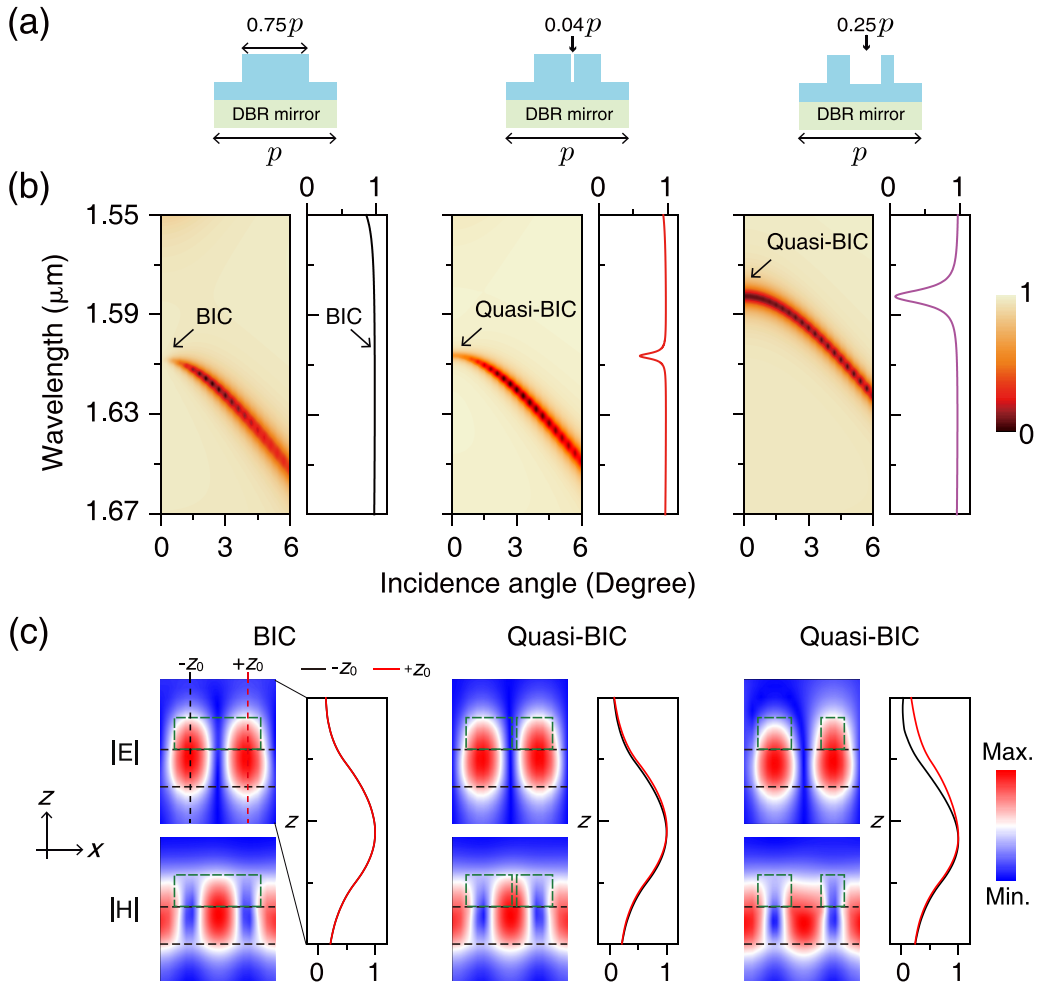

FIG. 3. (a) Side views of the symmetric grating (left) and the symmetry-broken dimerized grating (middle and right) deposited atop a DBR mirror. All three grating structures have a periodicity of $p = 800\,\text{nm}$. The stripe width of the symmetric grating is $0.75p$. For the symmetry-broken dimerized gratings, the air gaps are slightly offset from the center of the stripe by $0.04p$, with widths of $0.04p$ (middle) and $0.25p$ (right) respectively. (b) Reflection bands and (c) field profiles in the unit lattice for BIC (left) and quasi-BIC (middle and right).

In order for the quasi-BIC to radiate in only one port, the DBR must be completely reflective of light, i.e., DBR band gap. A DBR consists of multiple layers of two materials with different refractive indices, whose reflective properties depend on the material index n, thickness, and number of pairs of DBR. In general, the higher the refractive index contrast, the more broadband reflection can be achieved. To approach near perfect reflection, the more pairs of DBR would be beneficial. The quarter-wavelength thickness is required to achieve DBR band gap at the target wavelength λ_0, $\lambda_0/4n$. In this work, Si_3N_4/SiO_2 is considered due to the feasibility of both materials in nanofabrication. The target center wavelength is focused on the 1.55 μm communication band. This naturally leads to a thickness of 192 nm for Si_3N_4 layer and 268 nm for SiO_2 layer for an optimal band gap of Si_3N_4/SiO_2 DBR. From Fig. 2(b), it can be seen that an almost perfect band gap emerges at normal incidence in the wavelength range from 1.45 to 1.7 μm for nine pairs of Si_3N_4/SiO_2 DBR. So the quasi-BIC structure has only one backward reflecting port. For 1D symmetry-broken dimerized lattice structure, the structure parameters are set as follows: $p = 800\,\text{nm}$, $d = 200\,\text{nm}$, $g = 200\,\text{nm}$, $h_g = 220\,\text{nm}$, and $h_s = 270\,\text{nm}$.

To confirm the radiation engineering capability through our proposed quasi-BIC structure, we first focus on the symmetric grating and asymmetric dimerized grating deposited atop a DBR, whose side view shown in Fig. 3(a). For an optical resonance structure, it satisfies $R + T + A = 1$. If the quasi-BIC structure is lossless ($A = 0$), then this results in all light being reflected back ($R = 1$) due to the presence of DBR mirror ($T = 0$), making the optical mode *invisible*. Thus, to *see* the quasi-BIC resonance mode of a single-port quasi-BIC structure, there are two possible ways. One is to destroy the single-port system by decreasing the pair number of the DBR so that the leaky quasi-BIC can become *visible*. The evolution of the quasi-BIC spectra with the pair number of the DBR is shown in the Supplemental Material [36]. The other is to introduce some loss. Here, the latter is chosen for a more accurate and clearer view of the quasi-BIC. A weak loss is simply introduced by an increase in the imaginary part n_i of LN with $n_i = 0.002$. Figure 3(b) shows the corresponding reflection bands of the symmetric and asymmetric structures in Fig. 3(a) (lossless results shown in the Supplemental Material [36]). The leaky guided resonances from grating lattice scattering can be clearly observed [37], but disappear at normal

incidence for the symmetric grating with stripe width $0.75p$, as shown in the left of Fig. 3(b). This indicates the existence of symmetric-protected BIC at-Γ point [26]. When introducing a small gap perturbation (gap width $0.04p$) into the unit lattice of symmetric grating, the symmetry of the grating is broken and it becomes a symmetry-broken dimerized lattice structure. The reflection band retains the tendency of the original symmetric grating, with the exception of the symmetric-protected BIC at Γ point, which transforms into a quasi-BIC with a finite radiation capability, as shown in the middle of Fig. 3(b). When increasing gap perturbation (gap width $0.25p$), the bandwidth of the symmetric-broken quasi-BIC at Γ point becomes wider, indicating a further increase in its radiation capability, as shown in the right of Fig. 3(b). Figure 3(c) further demonstrates the similarity of the electric and magnetic field profiles between BIC and quasi-BIC. For the BIC, the symmetry of the field is identical to that of its own grating structure. With increasing gap perturbation, i.e., breaking the grating structure symmetry, the field becomes more asymmetric, forming a leaky quasi-BIC. Therefore, we demonstrate the existence of quasi-BIC in the asymmetric dimerized grating structure, originating from the distortion of the symmetric-protected BIC in the symmetric grating structure.

The radiation capability of the quasi-BIC may be extensively adjusted by asymmetric parameter. For our proposed quasi-BIC dimerized lattice structure, the asymmetric parameter is changing the widths of two stripes, denoted by $\delta = \triangle d/d$. As changing asymmetric parameter, the size of gap width g is always $0.25p$. The quasi-BIC in the right of Fig. 3 is a situation in the process of changing the asymmetric parameters. The specific quantitative relationship between radiation rate γ_r of quasi-BIC and asymmetric parameter δ is explored as follows. Figures 4(a) and 4(b) show the reflection spectra of at-Γ quasi-BIC as a function of wavelength and δ (the detailed results of the evolution of the reflection band and field profiles shown in the Supplemental Material [36]). The corresponding reflection spectra of the lossless quasi-BIC structure (the detailed result of spectra evolution shown in the Supplemental Material [36]) are also shown in Fig. 4(b) (dashed curves). It is found that the reflection spectra of symmetric-broken quasi-BIC show an increasing bandwidth with the evolution of δ. Noted that the resonance dip of the quasi-BIC vanishes for the symmetric structure $\delta = 0$. This is a special case of another symmetric grating with periodicity $p/2$ and strip width d, different from the one shown in the left of Fig. 3. The guided resonance of this special symmetric grating with periodicity $p/2$ could not be excited due to the mismatch with reciprocal lattice vector, actually corresponding to trapped mode or bound state below light cone. The origin of the quasi-BIC in dimerized lattice structure with periodicity p can be also thought of as bound state in symmetric grating with periodicity $p/2$ being folded into the continuum by periodic weak scattering. The asymmetric parameter δ actually corresponds to the ability of periodic weak scattering. The larger the δ, the more likely it is that the bound state will radiate out, giving a higher radiation rates γ_r. The values of γ_r of the quasi-BIC can be extracted by fitting absorption spectra with the CMT. As show in Fig. 4(c), the theory agrees excellently with the simulation result for the case of $\delta = 0.2$. Figure 4(d) summarizes γ_r of the quasi-BIC resonance as a function of δ.

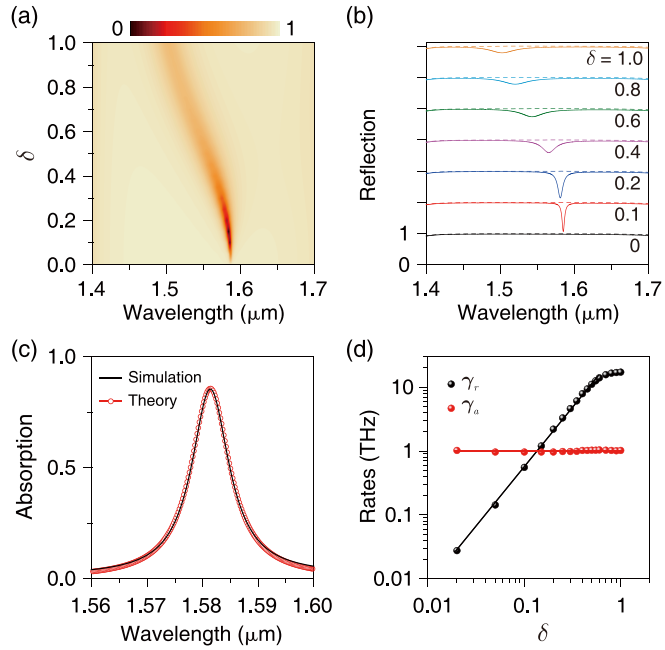

FIG. 4. (a), (b) Evolution of the reflection spectra of the quasi-BIC structure (with weak loss by introducing the imaginary part $n_i = 0.002$ of LN) under normal incidence with respect to wavelength and structure asymmetry parameter δ. The dashed curves in panel (b) show the reflection spectra of the lossless quasi-BIC structure. (c) Simulated reflection spectrum (black curve) of the quasi-BIC structure with $\delta = 0.2$ and fitted result by the CMT (red dotted curve). (d) Radiation rate γ_r and absorption rate γ_a of the quasi-BIC resonance as a function of δ (log-log scale). It shows almost unchanged γ_a and quadratic scalability of γ_r of quasi-BIC on δ.

A quadratic dependence of γ_r for small perturbation δ (below 0.6) can be clearly observed. The quadratic scalability of γ_r of quasi-BIC becomes weak for $\delta > 0.6$, but γ_r still increases with δ. This is consistent with the theoretical derivation of γ_r of quasi-BIC in Eq. (9). It is found that γ_r can be adjusted by over three orders of magnitude by changing δ from 0 to 1. This is likely to facilitates perfect absorber with precise and substantial adjustment of the bandwidth.

IV. BROADBAND AND NARROWBAND ABSORPTION PERFORMANCE

To construct a critical coupling system, graphene as a lossy component is integrated into the proposed quasi-BIC dimerized lattice structure. As shown in Fig. 2(a), graphene is sandwiched between the dimerized LN grating and the unetched LN film. The thickness and optical constant of graphene are adopted from Ref. [38]. From the above theory, it is clear that to broaden the absorption bandwidth of an absorber with optimal efficiency, it needs to increase γ_a and to satisfy the critical coupling condition $\gamma_a = \gamma_r$. An effective way to increase γ_a of graphene is increasing its layer numbers L. The absorption spectra of graphene with different L as a function of the asymmetric parameter δ and wavelength are shown in Fig. 5. From Figs. 5(a)–5(e), L are 1, 3, 6, 9, and 12, respectively. It can be seen that the absorption of bare graphene without the quasi-BIC dimerized

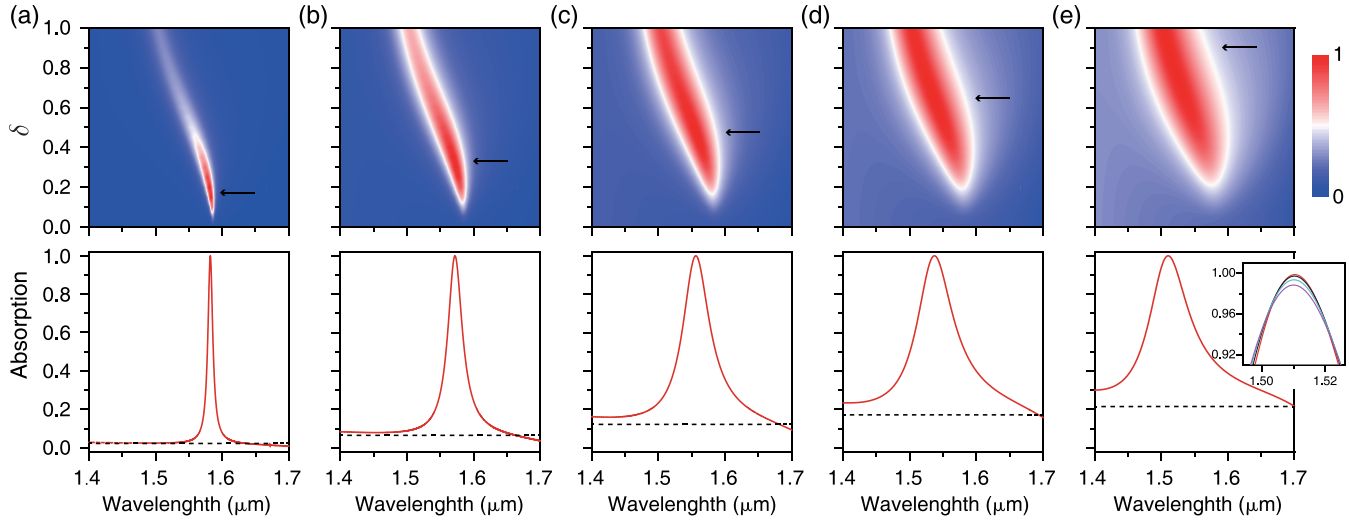

FIG. 5. (a)–(e) Absorption spectra of graphene with different layers L as a function of wavelength and structure asymmetry parameter δ (upper), and corresponding graphene absorption at critical coupling (lower). From panels (a)–(e), L are 1, 3, 6, 9, and 12, respectively. The corresponding critical coupling conditions are $\delta = 0.175$, 0.32, 0.475, 0.64, and 0.9, respectively, which are marked by black arrows (upper). The black dashed curves show the absorption of bare graphene with different L (lower). Inset in panel (e) shows detailed maximum absorption of graphene for $L = 12$ (red curve), 13 (black curve), 14 (blue curve), and 15 (purple curve).

lattice structure is proportional to L's. Through coupling with the quasi-BIC dimerized lattice structure, the absorption efficiency of graphene can be dramatically enhanced, even approaching perfect absorption at critical coupling. The critical coupling points for different L (marked by arrows in Fig. 5) can be found by adjusting the asymmetric parameter δ. Importantly, δ required to achieve perfect absorption at critical coupling of graphene increases with its L. This is because increasing graphene layers L corresponds to an increase in γ_a, so that a larger γ_r, corresponding to a larger asymmetric parameter δ, is required to match the critical coupling. In addition to achieving perfect absorption by integrating with the quasi-BIC dimerized lattice structure, the absorption bandwidth Γ^{FWHM} of graphene, typically at critical coupling can be also continuously broadened with increasing L. For monolayer graphene, its critical coupling condition occurs at $\delta = 0.175$, and the absorption bandwidth Γ^{FWHM} is only about 10 nm. The maximum L of graphene for which critical coupling could still be maintained (at $\delta = 0.9$) is 12, and the corresponding Γ^{FWHM} is increased up to 11 times that of the monolayer graphene case. By further increasing the layer numbers L of graphene ($L > 12$), the absorption efficiency starts to deviate slightly from perfect absorption at critical coupling, but Γ^{FWHM} can still be further increased. As can be seen from Fig. 1(c), to decrease the absorption efficiency, a large difference between γ_a and γ_r is required. Therefore, it is highly possible to continue increasing L of graphene to broaden Γ^{FWHM} while maintaining a near perfect absorption.

Except for broadband absorbers with high efficiency, the narrow-band and ultra-narrow-band absorbers are also important for such fields as selective filter [39], sensitive sensor [40] or active switch [41]. Following the strategy of tailoring bandwidth, to narrow down absorption bandwidth, both the radiation rate γ_r of the quasi-BIC and the absorption rate γ_a of graphene should be reduced simultaneously under the critical coupling condition. To decrease γ_r, the high-Q (quality factor) quasi-BIC induced by slightly breaking structure symmetry is preferentially used. However, there seems to be a limit for γ_a, as it is directly determined by the amount of absorbing material, and the minimum γ_a seems to be the monolayer graphene case. If γ_a cannot be decreased further, then it would make a mismatch with γ_r, certainly depressing the absorption performance. It is interesting that γ_a of the absorbing material is also influenced by the field distribution of the resonance mode, and can therefore be altered by varying the position of monolayer graphene in the quasi-BIC structure. The distance of monolayer graphene outwards away from the unetched LN film in the proposed quasi-BIC dimerized lattice structure is denoted as D. Figure 6 shows the absorption spectra of monolayer graphene with different D as a function of the asymmetric parameter δ and wavelength. As in the case of the broadband absorber, the critical coupling points for different D's can also be determined. It can be seen that the absorption bandwidth Γ^{FWHM} of monolayer graphene with perfect absorption can be adjusted substantially. Obviously, it shows an decrease of Γ^{FWHM} with increasing D. From the field distribution of the quasi-BIC distribution in Fig. 3(c), the field energy of the quasi-BIC is mainly stored inside the dimerized lattice structure. It indicates that the further away from the high-intensity field region of the quasi-BIC (with increasing D), the fewer photons could be absorbed by monolayer graphene, which naturally leads to an effective decrease in γ_a. Therefore, to realize perfect absorption at critical coupling condition $\gamma_r = \gamma_a$, it needs to decrease γ_r corresponding to lower asymmetric parameter δ. From Figs. 6(a)–6(d), the critical coupling conditions occur specifically at $\delta = 0.175$ for $D = 0$ nm, $\delta = 0.08$ for $D = 220$ nm, $\delta = 0.035$ for $D = 350$ nm, and $\delta = 0.012$ for $D = 500$ nm, respectively. The corresponding rates can be extracted as $\gamma_a = \gamma_r = 1.58$, 0.35, 0.0775, and 0.0105 THz, respectively. The absorption bandwidth of monolayer graphene at critical coupling could be shrunk over two orders of magnitude from 10

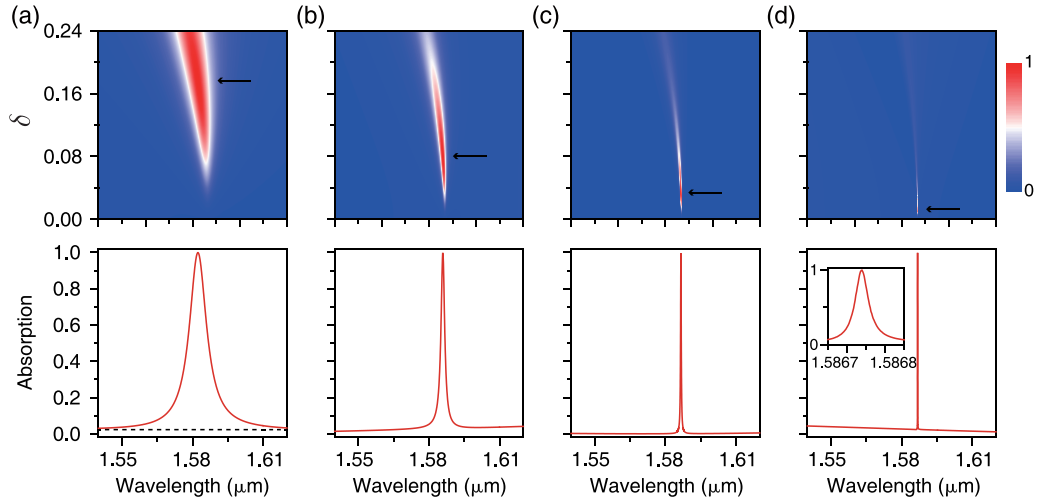

FIG. 6. (a)–(d) Absorption spectra of graphene with different positions D as a function of wavelength and structure asymmetry parameter δ (upper), and corresponding graphene absorption at critical coupling (lower). From panels (a)–(d), D are 0, 220, 350, and 500 nm, respectively. The corresponding critical coupling conditions are $\delta = 0.175$, 0.08, 0.035, and 0.012, respectively, which are marked by black arrows (upper). The black dashed curve in panel (a) shows the absorption of bare monolayer graphene. Inset in panel (d) shows detailed maximum absorption of graphene for $D = 500$ nm.

to 0.09 nm. Thus, by simultaneously adjusting the asymmetric parameter δ of the quasi-BIC structure and the positions D of monolayer graphene in the structure, the narrow-band or even ultra-narrow-band absorption of graphene with perfect absorption can be realized.

To visually compare the functionality in tailoring absorption of graphene, Fig. 7 summarizes the results shown in Figs. 5 and 6. The broadband absorption of graphene at critical coupling with different layers L and narrow-band absorption at different positions D are shown in the upper and lower panels of Fig. 7(a). The wavelength of each absorption spectrum is normalized by its own resonance wavelength λ/λ_0. It can be clearly found that Γ^{FWHM} of graphene at critical coupling can be sufficiently adjusted by changing its layers L or positions D in the quasi-BIC structure. The corresponding γ_a and γ_r as a function of L (grey-green area) or D (purple area) are shown in Fig. 7(b). The intersection of two coloured areas corresponds to that of monolayer graphene intercalated

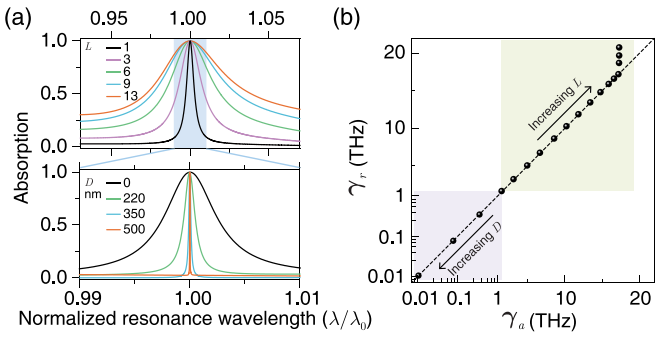

FIG. 7. (a) Critical coupling absorption of graphene with different layers L (upper) or different positions D (lower) in the quasi-BIC structure versus normalized resonance wavelength. (b) Decay rates of graphene with different L and D in the quasi-BIC structure fitted from the spectra in Figs. 5 and 6 via the CMT. The arrows show the trend of increasing L and D, respectively.

between the dimerized LN grating and the unetched LN film. The arrows represent the trend of increasing L and D, respectively. As increasing L or D, both rates are tailored along the line of the critical coupling $\gamma_a = \gamma_r$, and the perfect absorber is always achieved. The difference is that the total damping rate $\gamma_a + \gamma_r$ is manipulated in the opposite direction. For increasing graphene layers L from 1 to 12, the total damping rate $\gamma_a + \gamma_r$ is effectively increased. When increasing to 13 layers of graphene, the graphene absorber transfers into the undercoupling regime ($\gamma_a > \gamma_r$), but can maintain an absorption efficiency close to 100%. Importantly, $\gamma_a + \gamma_r$ is still increased with L, indicating a continuous increase in the absorption bandwidth. On the other hand, for increasing D of graphene, i.e., further away from the strong field area of the quasi-BIC, $\gamma_a + \gamma_r$ is decreased, indicating a narrower bandwidth. It can be predicted that, since γ_r of the quasi-BIC could be adjusted down to zero (BIC) by slightly breaking structure symmetry, Γ^{FWHM} could be infinitely narrow. This requires γ_a to be close to zero, corresponding to graphene located in the ultra-weak field area. These results demonstrate the powerful ability of the quasi-BIC to manipulate the absorption bandwidth over a wide range.

To investigate the dependence of the absorption bandwidth Γ^{FWHM} on the asymmetry parameter δ, Γ^{FWHM} of graphene with different layers L and its positions D in the quasi-BIC structure are extracted from the absorption spectra in Figs. 5 and 6, respectively. As can be seen from Fig. 8, the values of Γ^{FWHM} are well fitted by the square of δ (orange line), demonstrating the tailored quadratic dependence of Γ^{FWHM} on δ. The dependence of Γ^{FWHM} on δ exhibits a similar behavior, but shifted with value of $\lg 4$ relative to that of the radiation rate γ_r. The result verifies our theoretical derivation in Eq. (8) that gives $\lg \Gamma^{\mathrm{FWHM}} = \lg 4 + \lg \gamma_r$. It is worth noting that the quadratic scalability of the absorption bandwidth at critical coupling on the asymmetry parameter is essentially governed by the powerful physics of the symmetry-broken BIC in radiation engineering, which is in principle not

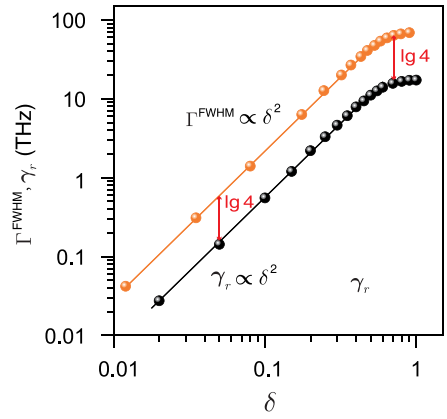

FIG. 8. Dependence of the absorption bandwidth Γ^{FWHM} of the quasi-BIC-governed graphene absorber at critical coupling and γ_r of the quasi-BIC resonance on the structure asymmetry parameter δ.

limited to a leaky guide mode in the dimerized lattice structure in this work, but is actually applicable to others such as trapped modes or supercavity modes in plasmonic and dielectric structures [42–44]. Meanwhile, this concept could also be applied to other absorbing materials such as transition-metal dichalcogenides [45] and black phosphorus [46]. Therefore, the proposed BIC-inspired strategy for tailoring optimal absorber shows general applicability, possibly providing an efficient approach for the design of next-generation photonic devices.

The angular dependence of the quasi-BIC-governed graphene absorber at critical coupling is further investigated. Figures 9(a) and 9(b) show the broadband case in Fig. 5(e) and the narrow-band case in Fig. 6(b), respectively. It can be seen that both broadband and narrow-band quasi-BIC-governed graphene absorbers exhibit an almost perfect absorption response over a wide angular range. At incidence angle above 18 degrees, the absorption efficiency and bandwidth drop off rapidly. This is because that the dispersion band of the quasi-BIC extends beyond the DBR band gap, giving the quasi-BIC another forward leaky port. As a result, the whole quasi-BIC-

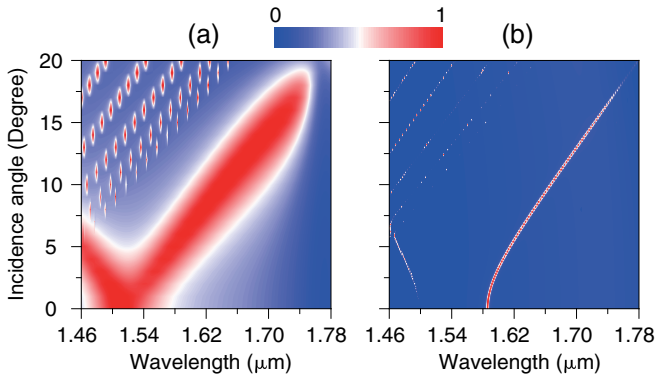

FIG. 9. (a) Broadband and (b) narrow-band light absorption of quasi-BIC-governed graphene absorber at critical coupling as a function of wavelength and incidence angle. The critical coupling structures in panels (a) and (b) are the same as Figs. 5(e) and 6(b), respectively.

governed graphene absorber with another leaky port cannot fulfill the perfect absorption condition in a single port. This result is consistent with our theoretical analysis in Eq. (6) that the maximum absorption efficiency of a single optical resonator is inversely proportional to its port number m. The role of the DBR as a mirror therefore strongly influences the absorption performance. The absorption spectra of graphene as a function of the pair number of the DBR are shown in the Supplemental Material [36]. It can be seen that the reflection of the DBR, in particular the absorption efficiency of graphene increases in the pair number of the DBR. The perfect absorption can be achieved when the DBR behaves as a fully reflective mirror. The absorption performance can also be adjusted by introducing a DBR defect mode (shown in the Supplemental Material [36]). It suggests that the DBR defect mode allows the quasi-BIC to leak out toward the DBR, resulting in lower absorption (see Supplemental Material [36]).

V. CONCLUSION

In conclusion, we derive the key parameters determining absorption performance, i.e., absorption efficiency and absorption bandwidth of an optical absorber, and link it with radiation engineering of the symmetry-broken quasi-BIC. Based on this, we propose a BIC-inspired strategy to tailor light absorption at critical coupling. Taking absorbing material graphene integrated with the lossless symmetry-broken dimerized lattice structure deposited atop a DBR as a model, the manipulation of the broadband or narrow-band quasi-BIC-governed graphene absorber with perfect absorption is demonstrated. By simultaneously adjusting the layer number of graphene and the asymmetry parameter of the quasi-BIC structure, the absorption bandwidth of the quasi-BIC-governed perfect absorber can be increased up to 11 times. Meanwhile, by adjusting the position of monolayer graphene in the quasi-BIC structure, the perfect absorber with more than two orders of bandwidth decrease can also be realized. We predict and verify that the absorption bandwidth at critical coupling is quadratically tailored as a function of the asymmetry parameter, which essentially arises from the robust physics of BIC in radiation engineering. The proposed BIC-inspired strategy shows general applicability in different physical implementations of critical coupling systems, in principle, that atomically thin 2D materials integrated with various symmetry-broken quasi-BIC structures. This work therefore would offer a scheme for the development of high-performance devices with flexibility such as photodetectors, modulators, and sensors.

ACKNOWLEDGMENTS

The work was supported by the National Natural Science Foundation of China (Grants No. 12204499 and No. 62075225), Joint Key Projects of National Natural Science Foundation of China (Grant No. U2032206), CAS Project for Young Scientists in Basic Research (Grant No. YSBR-042), and Open Project of State Key Laboratory of Surface Physics in Fudan University (Grant No. KF2022_05). The authors thank the staff from BL06B beamline of Shanghai Synchrotron Radiation Facility (SSRF) for helpful discussions.

[1] O. Neumann, A. S. Urban, J. Day, S. Lal, P. Nordlander, and N. J. Halas, Solar vapor generation enabled by nanoparticles, ACS Nano **7**, 42 (2013).

[2] X. Zhu, C. Vannahme, E. Højlund-Nielsen, N. A. Mortensen, and A. Kristensen, Plasmonic colour laser printing, Nat. Nanotechnol. **11**, 325 (2016).

[3] J. Oh, H.-C. Yuan, and H. M. Branz, An 18.2%-efficient black-silicon solar cell achieved through control of carrier recombination in nanostructures, Nat. Nanotechnol. **7**, 743 (2012).

[4] M. Algasinger, J. Paye, F. Werner, J. Schmidt, M. S. Brandt, M. Stutzmann, and S. Koynov, Improved black silicon for photovoltaic applications, Adv. Energy Mater. **3**, 1068 (2013).

[5] J. R. Piper and S. Fan, Broadband absorption enhancement in solar cells with an atomically thin active layer, ACS Photon. **3**, 571 (2016).

[6] J. Wang, J. Yang, and D. Shi, Perfect absorption for monolayer transition-metal dichalcogenides by critical coupling, Nanotechnology **31**, 465205 (2020).

[7] S. Xiao, T. Liu, X. Wang, X. Liu, and C. Zhou, Tailoring the absorption bandwidth of graphene at critical coupling, Phys. Rev. B **102**, 085410 (2020).

[8] H. Li, M. Qin, L. Wang, X. Zhai, R. Ren, and J. Hu, Total absorption of light in monolayer transition-metal dichalcogenides by critical coupling, Opt. Express **25**, 31612 (2017).

[9] C. Qu, S. Ma, J. Hao, M. Qiu, X. Li, S. Xiao, Z. Miao, N. Dai, Q. He, S. Sun *et al.*, Tailor the functionalities of metasurfaces based on a complete phase diagram, Phys. Rev. Lett. **115**, 235503 (2015).

[10] Y. Xia, J. Wang, Y. Zhang, Y. Shan, Y. Dai, A. Chen, T. Shen, S. Wu, X. Liu, L. Shi *et al.*, Transmission-type optical modulator based on graphene plasmonic resonator integrated with off-resonant Au structure, Adv. Opt. Mater. **8**, 2000264 (2020).

[11] T. Liu, X. Jiang, H. Wang, Y. Liu, C. Zhou, and S. Xiao, Tunable anisotropic absorption in monolayer black phosphorus using critical coupling, Appl. Phys. Express **13**, 012010 (2019).

[12] M. Islam, J. Sultana, M. Biabanifard, Z. Vafapour, M. Nine, A. Dinovitser, C. Cordeiro, B.-H. Ng, and D. Abbott, Tunable localized surface plasmon graphene metasurface for multiband superabsorption and terahertz sensing, Carbon **158**, 559 (2020).

[13] M. Zhou, L. Shi, J. Zi, and Z. Yu, Extraordinarily large optical cross section for localized single nanoresonator, Phys. Rev. Lett. **115**, 023903 (2015).

[14] J. Wang, D. Han, A. Chen, Y. Dai, M. Zhou, X. Hu, Z. Yu, X. Liu, L. Shi, and J. Zi, Using active gain to maximize light absorption, Phys. Rev. B **96**, 195419 (2017).

[15] V. Grigoriev, N. Bonod, J. Wenger, and B. Stout, Optimizing nanoparticle designs for ideal absorption of light, ACS Photon. **2**, 263 (2015).

[16] L. Meng, D. Zhao, Y. Yang, F. J. G. De Abajo, Q. Li, Z. Ruan, and M. Qiu, Gain-assisted plasmon resonance narrowing and its application in sensing, Phys. Rev. Appl. **11**, 044030 (2019).

[17] Y. Cui, K. H. Fung, J. Xu, H. Ma, Y. Jin, S. He, and N. X. Fang, Ultrabroadband light absorption by a sawtooth anisotropic metamaterial slab, Nano Lett. **12**, 1443 (2012).

[18] K. Aydin, V. E. Ferry, R. M. Briggs, and H. A. Atwater, Broadband polarization-independent resonant light absorption using ultrathin plasmonic super absorbers, Nat. Commun. **2**, 517 (2011).

[19] L. Huang, G. Li, A. Gurarslan, Y. Yu, R. Kirste, W. Guo, J. Zhao, R. Collazo, Z. Sitar, G. N. Parsons *et al.*, Atomically thin MoS_2 narrowband and broadband light superabsorbers, ACS Nano **10**, 7493 (2016).

[20] X. Chen, Q. Meng, W. Xu, J. Zhang, Z. Zhu, and S. Qin, Electrically tunable absorber based on a graphene integrated lithium niobate resonant metasurface, Opt. Express **29**, 32796 (2021).

[21] K. Sun, Z. Zhao, Y. Cai, U. Levy, and Z. Han, Ultra-narrowband and highly-directional THz thermal emitters based on the bound state in the continuum, Nanophotonics **10**, 4035 (2021).

[22] L. Meng, D. Zhao, Z. Ruan, Q. Li, Y. Yang, and M. Qiu, Optimized grating as an ultra-narrow band absorber or plasmonic sensor, Opt. Lett. **39**, 1137 (2014).

[23] K. Koshelev, S. Lepeshov, M. Liu, A. Bogdanov, and Y. Kivshar, Asymmetric metasurfaces with high-Q resonances governed by bound states in the continuum, Phys. Rev. Lett. **121**, 193903 (2018).

[24] S. Joseph, S. Pandey, S. Sarkar, and J. Joseph, Bound states in the continuum in resonant nanostructures: An overview of engineered materials for tailored applications, Nanophotonics **10**, 4175 (2021).

[25] S. Campione, S. Liu, L. I. Basilio, L. K. Warne, W. L. Langston, T. S. Luk, J. R. Wendt, J. L. Reno, G. A. Keeler, I. Brener *et al.*, Broken symmetry dielectric resonators for high quality factor Fano metasurfaces, ACS Photon. **3**, 2362 (2016).

[26] C. W. Hsu, B. Zhen, A. D. Stone, J. D. Joannopoulos, and M. Soljačić, Bound states in the continuum, Nat. Rev. Mater. **1**, 16048 (2016).

[27] B. Zhen, C. W. Hsu, L. Lu, A. D. Stone, and M. Soljačić, Topological nature of optical bound states in the continuum, Phys. Rev. Lett. **113**, 257401 (2014).

[28] S. Mohamed, J. Wang, H. Rekola, J. Heikkinen, B. Asamoah, L. Shi, and T. K. Hakala, Controlling topology and polarization state of lasing photonic bound states in continuum, Laser Photon. Rev. **16**, 2100574 (2022).

[29] C. W. Hsu, B. Zhen, J. Lee, S.-L. Chua, S. G. Johnson, J. D. Joannopoulos, and M. Soljačić, Observation of trapped light within the radiation continuum, Nature (London) **499**, 188 (2013).

[30] H. A. Haus, *Waves and Fields in Optoelectronics* (Prentice Hall, Englewood Cliffs, NJ, 1984).

[31] S. Fan, W. Suh, and J. D. Joannopoulos, Temporal coupled-mode theory for the Fano resonance in optical resonators, J. Opt. Soc. Am. A **20**, 569 (2003).

[32] Z. Yu, A. Raman, and S. Fan, Fundamental limit of nanophotonic light trapping in solar cells, Proc. Natl. Acad. Sci. USA **107**, 17491 (2010).

[33] J. Wang, A. Chen, Y. Zhang, J. Zeng, Y. Zhang, X. Liu, L. Shi, and J. Zi, Manipulating bandwidth of light absorption at critical coupling: An example of graphene integrated with dielectric photonic structure, Phys. Rev. B **100**, 075407 (2019).

[34] A. C. Overvig, S. Shrestha, and N. Yu, Dimerized high contrast gratings, Nanophotonics **7**, 1157 (2018).

[35] M. G. Moharam and T. K. Gaylord, Rigorous coupled-wave analysis of planar-grating diffraction, J. Opt. Soc. Am. **71**, 811 (1981).

[36] See Supplemental Material at http://link.aps.org/supplemental/10.1103/PhysRevB.108.205428 for more detailed results.

[37] S. H. Fan and J. D. Joannopoulos, Analysis of guided resonances in photonic crystal slabs, Phys. Rev. B **65**, 235112 (2002).

[38] M. Bruna and S. Borini, Optical constants of graphene layers in the visible range, Appl. Phys. Lett. **94**, 031901 (2009).

[39] X. J. Wang, H. Y. Meng, S. Liu, S. Y. Deng, T. Jiao, Z. C. Wei, F. Q. Wang, C. H. Tan, and X. G. Huang, Tunable graphene-based mid-infrared plasmonic multispectral and narrow band-stop filter, Mater. Res. Express **5**, 045804 (2018).

[40] J. Wang, J. Yang, H. Zhao, and M. Chen, Quasi-BIC-governed light absorption of monolayer transition-metal dichalcogenide-based absorber and its sensing performance, J. Phys. D: Appl. Phys. **54**, 485106 (2021).

[41] Z. Song, A. Chen, and J. Zhang, Terahertz switching between broadband absorption and narrowband absorption, Opt. Express **28**, 2037 (2020).

[42] G. Zhang, C. Lan, R. Gao, and J. Zhou, Trapped-mode-induced giant magnetic field enhancement in all-dielectric metasurfaces, J. Phys. Chem. C **123**, 28887 (2019).

[43] M. V. Rybin, K. L. Koshelev, Z. F. Sadrieva, K. B. Samusev, A. A. Bogdanov, M. F. Limonov, and Y. S. Kivshar, High-Q supercavity modes in subwavelength dielectric resonators, Phys. Rev. Lett. **119**, 243901 (2017).

[44] S. Droulias, S. Mohamed, H. Rekola, T. K. Hakala, C. M. Soukoulis, and T. Koschny, Experimental demonstration of dark-state metasurface laser with controllable radiative coupling, Adv. Opt. Mater. **10**, 2102679 (2022).

[45] E. Barré, O. Karni, E. Liu, A. L. OBeirne, X. Chen, H. B. Ribeiro, L. Yu, B. Kim, K. Watanabe, T. Taniguchi *et al.*, Optical absorption of interlayer excitons in transition-metal dichalcogenide heterostructures, Science **376**, 406 (2022).

[46] S. Huang and X. Ling, Black phosphorus: Optical characterization, properties and applications, Small **13**, 1700823 (2017).